Nonlinear Dynamics (2026) 114:1232
https://doi.org/10.1007/s11071-026-13128-w

RESEARCH

A stable exceptional point reorganizes relaxation before the Hopf bifurcation to a breathing chimera

Ehsan Bolhasani[1] · **Seyed Hamed Aboutalebi**[2,3] · **Matjaž Perc**[4,5,6,7]

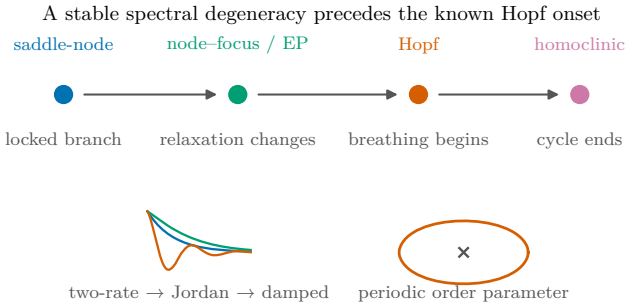
Received: 7 August 2026 / Revised: 21 September 2026 / Accepted: 4 October 2026
© The Author(s), under exclusive licence to Springer Nature B.V. 2026

Abstract

Breathing chimeras arise through a Hopf bifurcation in the two-population Kuramoto–Sakaguchi reduction. On the preceding stable locked-chimera branch, we identify a defective node–focus transition, equivalently a second-order exceptional point of the reduced Jacobian. Two negative eigenvalues and their eigenvectors coalesce while the locked chimera remains hyperbolic and stable. This spectral degeneracy is not a bifurcation. It changes linear relaxation from a bi-exponential return, through a Jordan response, to damped oscillations, distinguishing collective ringing from self-sustained breathing. The later supercritical Hopf bifurcation creates the breathing cycle; its nontrivial Floquet exponents in the Ott–Antonsen phase quotient are negative on the sampled breathing branch, and invariant-manifold shooting identifies its homoclinic termination. An elementary discriminant argument explains why a node–focus boundary is expected between saddle-node and Hopf for the same isolated pair. The contribution is its location, verified defectiveness and stability, and observable reduced relaxation. A moment-defect estimate quantifies finite-time departures from the reduction without assuming generic microscopic attraction. Small positive frequency dispersion preserves the event ordering. A Möbius phase reset realizes the coherence pulse at oscillator level, while finite-population observation of the post-pulse Jordan trace remains an open question.

Graphical abstract

The defective node–focus transition, equivalently a second-order exceptional point (EP) of the reduced Jacobian, changes stable relaxation; the later Hopf bifurcation creates breathing.



Keywords Chimera states · Exceptional points · Node–focus transition · Hopf bifurcation · Homoclinic bifurcation · Ott–Antonsen reduction

✉ Ehsan Bolhasani
e.bolhasani@phys.ui.ac.ir

✉ Matjaž Perc
matjaz.perc@gmail.com

[1] Department of Physics, University of Isfahan, Isfahan 81746-73441, Iran

[2] Condensed Matter National Laboratory, Institute for Research in Fundamental Sciences (IPM), Tehran 19395-5531, Iran

[3] School of Quantum Physics and Matter, Institute for Research in Fundamental Sciences (IPM), Tehran 19395-5531, Iran

[4] Faculty of Natural Sciences and Mathematics, University of Maribor, Koroška cesta 160, Maribor 2000, Slovenia

Published online: 15 October 2026

1 Introduction

Chimera states combine coherent and incoherent motion in networks of identical or nearly identical oscillators. The phenomenon was first identified in nonlocally coupled phase oscillators and subsequently developed in an analytically explicit ring setting [1–3]. It has since been followed across heterogeneous ensembles and varied interaction topologies [4, 5], while broad reviews chart the resulting range of chimera dynamics [6–9]. Experimental chimera states have been demonstrated in optical, chemical, and mechanical platforms [10–12], while breathing chimeras constitute a distinct dynamical regime in which the macroscopic order parameters oscillate periodically. A locked chimera has time-independent macroscopic order parameters, whereas a breathing chimera displays periodic modulation. Among the minimal settings for collective dynamics, two interacting oscillator populations provide a particularly transparent route from microscopic phase equations to macroscopic states [13]. For the canonical two-population Kuramoto–Sakaguchi model, Abrams et al. established the relevant saddle-node, Hopf, and homoclinic bifurcation structure and showed that breathing chimeras are created at the Hopf bifurcation [14]. Subsequent work examined spectral properties of chimera states, finite-population realizations, and the dynamics and stability of the two-population architecture [15–17], while breathing chimeras were studied as dynamical objects in their own right [18, 19]. The established Hopf onset is not reconsidered here. Instead, we ask a narrower question that was not addressed in the original bifurcation analysis: how do the stable decay modes of the locked branch reorganize before the known Hopf point?

The tractability of this question rests on low-dimensional reductions, but several notions of stability must be kept distinct. The Ott–Antonsen reduction captures macroscopic order-parameter dynamics [20, 21], whereas the Watanabe–Strogatz and Möbius descriptions expose constants of motion for identical oscillators [22–24]. Consequently, stability in the reduced phase quotient need not imply attraction from arbitrary microscopic phase distributions [25]. Finite two-population studies further distinguish Poisson from non-Poisson chimeras [26], and basin-based analyses quantify a global robustness that is different from local Jacobian stability [27, 28]. We therefore state the scope explicitly: the spectral event and its post-pulse relaxation are established in the Ott–Antonsen phase quotient. Finite-population tests check Poisson-prepared breathing cycles and the instantaneous reset, separately; they do not establish the microscopic post-pulse Jordan trace. The spectral event is also continued to small positive frequency dispersion.

Exceptional points are defective degeneracies at which eigenvalues and eigenvectors coalesce. They are well established in operator perturbation theory and non-Hermitian wave physics [29–31], and in dissipative-system Jacobians [32]. Exceptional points have also been linked to chimera emergence with nonreciprocal Stuart–Landau coupling [33]. Recent work on nonreciprocal active polar mixtures connects continuum exceptional points with microscopic collective motion [34]. These studies motivate distinguishing a spectral degeneracy from the physical process that it accompanies.

Here the exceptional point (EP) is the defective node–focus boundary of an already existing locked chimera with reciprocal population coupling. It remains hyperbolic and stable: the EP is not a bifurcation and does not cause breathing. Our contribution is to locate and verify this stable, spectrally isolated degeneracy, characterize the observable reduced return, and separate it quantitatively from Hopf. The distinction matters when interpreting an oscillatory recovery of coherence: a stable focus can ring after a perturbation without supporting a breathing attractor. The full three-dimensional Ott–Antonsen (OA) quotient at positive frequency dispersion tests persistence beyond the invariant coherent boundary.

For clarity, a *node* has two distinct real negative decay rates; a stable *focus* has a complex-conjugate pair with negative real part. Their *node–focus boundary* has a repeated real eigenvalue. It is *defective* when the eigenspace is one-dimensional, giving a second-order EP. The resulting *Jordan response* contains $te^{\lambda_* t}$ as well as $e^{\lambda_* t}$. A *breathing chimera*, in contrast, is a periodic macroscopic state after transients.

Figure 1 summarizes the event hierarchy on the fixed $\beta = 0.10$ parameter slice. The saddle-node bifurcation creates the locked branch, the stable EP changes its linear return, the Hopf bifurcation creates breathing, and the periodic branch terminates at a homoclinic bifurcation.

2 Model, phase quotient, and stated scope

Population $\sigma \in \{1, \ldots, M\}$ contains N_σ phase oscillators:

$$\dot{\theta}_i^\sigma = \omega_i^\sigma + \sum_{\tau=1}^{M} \frac{K_{\sigma\tau}}{N_\tau} \sum_{j=1}^{N_\tau} \sin(\theta_j^\tau - \theta_i^\sigma - \alpha_{\sigma\tau}). \tag{1}$$

This is the standard Kuramoto–Sakaguchi phase-oscillator coupling convention [35, 36]. For Lorentzian frequency distributions with center ω_σ and half-width Δ_σ, the OA order

5 Community Healthcare Center Dr. Adolf Drolc Maribor, Ulica talcev 9, Maribor 2000, Slovenia

6 Department of Physics, Kyung Hee University, Dongdaemun-gu, Seoul 02447, Republic of Korea

7 University College, Korea University, Seongbuk-gu, Seoul 02841, Republic of Korea

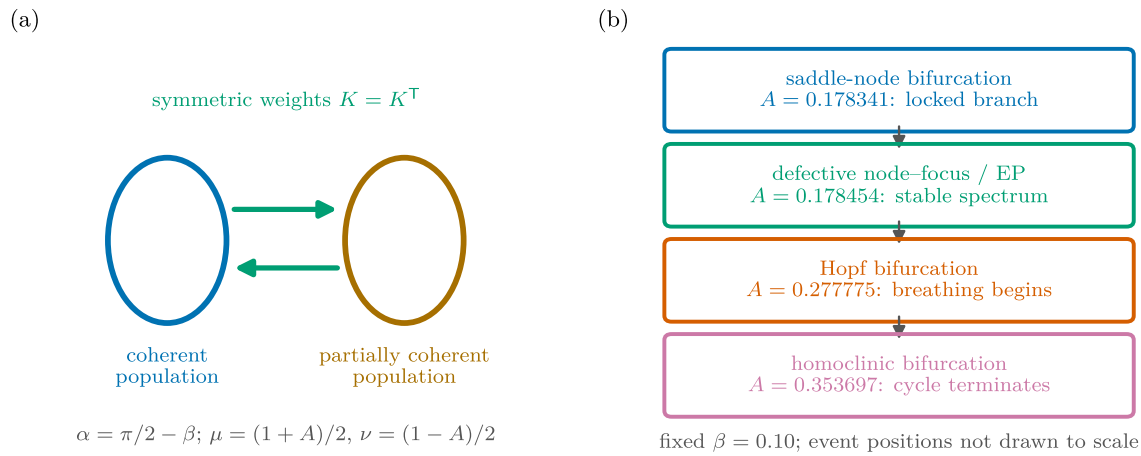


Fig. 1 Model and event hierarchy. **a** Two oscillator populations are coupled reciprocally with $\alpha = \pi/2 - \beta$, within-population weight $\mu = (1 + A)/2$, and between-population weight $\nu = (1 - A)/2$. **b** Along the fixed $\beta = 0.10$ slice, the saddle-node bifurcation (SN) creates the locked branch at $A_{\mathrm{SN}} = 0.178341$; the defective node–focus transition, equivalently a Jacobian exceptional point (EP), occurs at $A_{\mathrm{EP}} = 0.178454$; the Hopf bifurcation (H) creates a breathing chimera at $A_H = 0.277775$; and the periodic branch ends in a homoclinic bifurcation at $A_{\mathrm{hom}} = 0.353697$. Positions in the schematic are not to scale. Numerical sensitivity estimates for the event parameters are reported in Table 1; the six-decimal labels are rounded

parameters $z_\sigma = \rho_\sigma e^{i\phi_\sigma}$ satisfy [20, 21]

$$\dot{z}_\sigma = (-\Delta_\sigma + i\omega_\sigma) z_\sigma + \frac{1}{2} \sum_\tau K_{\sigma\tau} \left(e^{-i\alpha_{\sigma\tau}} z_\tau - e^{i\alpha_{\sigma\tau}} \bar{z}_\tau z_\sigma^2 \right). \tag{2}$$

Removing the neutral global phase gives a $(2M - 1)$-dimensional quotient in the amplitudes and $M - 1$ phase differences.

For the main two-population calculation, the two frequency centers are equal and their common value is removed in a co-rotating frame, so that $\omega_1 = \omega_2 = 0$. Moreover, $\Delta_1 = \Delta_2 = 0$, all four phase lags satisfy $\alpha_{\sigma\tau} = \alpha$, $\beta = \pi/2 - \alpha$, and

$$K = \begin{pmatrix} \mu & \nu \\ \nu & \mu \end{pmatrix}, \qquad \mu = \frac{1 + A}{2}, \quad \nu = \frac{1 - A}{2}. \tag{3}$$

On the invariant boundary $\rho_1 = 1$, let $r = \rho_2$ and $\psi = \phi_1 - \phi_2$. The exact planar quotient is

$$\dot{r} = \frac{1 - r^2}{2} [\mu r \sin\beta + \nu \sin(\psi + \beta)], \tag{4a}$$

$$\dot{\psi} = -\mu \cos\beta - \nu r \cos(\beta - \psi) + \frac{1 + r^2}{2r} [\mu r \cos\beta + \nu \cos(\psi + \beta)]. \tag{4b}$$

The instantaneous exponent normal to $\rho_1 = 1$ is

$$\lambda_\perp(t) = -[\mu \sin\beta + \nu r(t) \sin(\beta - \psi(t))]. \tag{5}$$

A step-by-step derivation from Eq. (2), including the proof of boundary invariance and the boundary-normal linearization, is given in Sec. S1 of Online Resource 1.

At zero frequency width, OA stability is not generic continuum stability. Watanabe–Strogatz constants survive, and the OA manifold need not attract arbitrary microscopic phase distributions [22, 24, 25]. Equilibrium and cycle stability below therefore refer to the OA phase quotient. The finite-N study uses Poisson-kernel initial samples and tests finite-horizon ensemble convergence for that preparation; it does not establish attraction from generic microscopic states.

2.1 Off-manifold departures and a finite-time estimate

An explicit closure defect makes this limitation quantitative. For identical frequencies in the co-rotating frame, define $Z_{\sigma,n} = \langle e^{in\theta^\sigma} \rangle$, $z_\sigma = Z_{\sigma,1}$, $H_\sigma = e^{-i\alpha} \sum_\tau K_{\sigma\tau} z_\tau$, and $\chi_\sigma = Z_{\sigma,2} - z_\sigma^2$. The exact first-moment equation is

$$\dot{z}_\sigma = \tfrac{1}{2}(H_\sigma - \bar{H}_\sigma z_\sigma^2) - \tfrac{1}{2} \bar{H}_\sigma \chi_\sigma. \tag{6}$$

It holds for empirical finite populations as well as continuum ensembles. The first term is the OA vector field; the second measures its instantaneous error. With the same initial first moments and $0 \le A \le 1$, the row sums of K are one. Hence $|H_\sigma| \le 1$ and the OA field is Lipschitz with constant at most 2 in the maximum norm on the product of unit disks. Writing $E(t) = \max_\sigma |z_\sigma(t) - z_\sigma^{\mathrm{OA}}(t)|$ and $\eta(t) = \max_\sigma |\chi_\sigma(t)|$,

Gronwall's inequality gives

$$E(t) \le \tfrac{1}{2} \int_0^t \mathrm{e}^{2(t-s)} \eta(s)\, ds. \tag{7}$$

This is a conservative a posteriori finite-time bound, not an attraction theorem: it needs control of higher moments along the actual trajectory and can become uninformative at long times. In particular, non-Poisson ensembles with identical initial z_σ can have different χ_σ and different returns. Section S5 of Online Resource 1 derives the estimate and gives such an explicit initial-distribution example.

For continuous nonzero frequency width, OA attraction results require regularity and analyticity hypotheses on the frequency-dependent density [21, 37]; they cannot be transferred unconditionally to the zero-width limit. Recent circular-cumulant work also illustrates how departures from OA closure affect collective dynamics under asymmetric noise [38]. That is a different model, not an attraction result for the noiseless chimera studied here. Our positive- dispersion continuation tests persistence within the OA quotient, not a uniform-in-dispersion error bound or a basin of microscopic attraction.

2.2 Order-parameter geometry

For metric-dependent decompositions we declare the order-parameter metric

$$ds^2 = \sum_{\sigma=1}^{M} |dz_\sigma|^2. \tag{8}$$

After minimization over global phase, its amplitude block is the identity and its phase block is

$$G_\psi = \operatorname{diag}(w_1, \ldots, w_{M-1}) - \frac{\boldsymbol{w}\boldsymbol{w}^{\mathsf{T}}}{\sum_{\sigma=1}^{M} w_\sigma}, \qquad w_\sigma = \rho_\sigma^2. \tag{9}$$

On the two-population boundary this gives $W = \operatorname{diag}(1, r^2/(1+r^2))$ in (r, ψ). Eigenvalues, the discriminant, and Jordan structure do not depend on this declaration; the numerical symmetric and skew-adjoint components do. Physically, this metric measures squared changes of the complex population coherences after removal of an irrelevant common phase. A phase change of an almost incoherent population receives a smaller weight because its complex order parameter changes little. It is not a metric on all microscopic distributions or on their Watanabe–Strogatz constants.

3 Restricted Jacobian and the continuity observation

Suppose a conjugation-invariant spectral pair of a real Jacobian $J(p) \in \mathbb{R}^{n\times n}$ is isolated along a branch. In coordinates normalized by the declared metric, an ordered real-Schur decomposition gives an orthonormal basis $Q \in \mathbb{R}^{n\times 2}$ and the exact linear restriction [29, 39]

$$JQ = QB, \qquad B = Q^{\mathsf{T}} J Q = \begin{pmatrix} a & b \\ c & d \end{pmatrix}. \tag{10}$$

This is an invariant linear two-mode description; it is not, without a separate invariant-manifold argument, a nonlinear planar reduction of the full system.

Write

$$B = \tau I + \begin{pmatrix} \delta & s \\ s & -\delta \end{pmatrix} + g \begin{pmatrix} 0 & 1 \\ -1 & 0 \end{pmatrix}, \tag{11}$$

where $\tau = (a+d)/2$, $\delta = (a-d)/2$, $s = (b+c)/2$, and $g = (b-c)/2$. Define $g_{\mathrm{s}} = (\delta^2 + s^2)^{1/2}$ and $g_{\mathrm{a}} = |g|$. Here g_{a} is the magnitude of the skew-adjoint component of the restricted Jacobian, and g_{s} is the magnitude of its traceless self-adjoint component, both in the declared metric. Direct multiplication gives

$$\lambda_\pm = \tau \pm \sqrt{g_{\mathrm{s}}^2 - g_{\mathrm{a}}^2}, \qquad \mathcal{D} = (\operatorname{tr} B)^2 - 4 \det B = 4(g_{\mathrm{s}}^2 - g_{\mathrm{a}}^2). \tag{12}$$

Thus $\mathcal{D} > 0$ is the node side, $\mathcal{D} < 0$ is the focus side, and a non-scalar block at $\mathcal{D} = 0$ is defective. The balance $g_{\mathrm{s}} = g_{\mathrm{a}}$ has a metric-independent zero set, although the two magnitudes separately depend on the metric. It is neither a criterion for structural nonreciprocity nor a system-wide instability measure.

Indeed, any positive-definite metric on the same two-mode space gives a nonsingular change of coordinates $\widetilde{B} = SBS^{-1}$. Trace, determinant, and Jordan structure are preserved, so $\widetilde{g}_{\mathrm{s}}^2 - \widetilde{g}_{\mathrm{a}}^2 = \mathcal{D}/4$. At the EP, the coordinate-Euclidean metric gives $g_{\mathrm{s}} = g_{\mathrm{a}} \simeq 0.042019$; the declared order-parameter metric gives $g_{\mathrm{s}} = g_{\mathrm{a}} \simeq 0.059111$ (Online Resource 1, Sect. S6), at the same A_{EP}. A description retaining additional Watanabe–Strogatz invariants enlarges the dynamical state space; it is not merely a different metric on this Jacobian.

Lemma 1 *(Discriminant sign change for a tracked pair) Let the same isolated real rank-two spectral bundle be followed continuously from a generic saddle-node, where its spectrum is* $\{0, \lambda_s\}$ *with* $\lambda_s \neq 0$*, to a nondegenerate Hopf point, where its spectrum is* $\{\pm \mathrm{i}\Omega_H\}$ *with* $\Omega_H > 0$*. Then its discriminant vanishes at least once between the endpoints. If the zero is*

transverse, the restricted matrix is non-scalar and defective, and its eigenvalue splitting is proportional to the square root of distance from the zero.

At the saddle-node $\mathcal{D} = \lambda_s^2 > 0$, whereas at Hopf $\mathcal{D} = -4\Omega_H^2 < 0$; the first statement is the intermediate value theorem. If B were scalar at a zero, then $\delta = s = g = 0$ and Eq. (12) would give $\mathcal{D}' = 0$, contradicting transversality. Finally, $\lambda_+ - \lambda_- = \sqrt{\mathcal{D}}$ gives the square-root splitting. This elementary node–focus observation is not itself the novelty. The model-specific consequences are established next.

4 A stable defective node–focus transition

At $\beta = 0.10$, augmented equilibrium solves locate

$$\begin{aligned} A_{\mathrm{SN}} &= 0.178341, \\ A_{\mathrm{EP}} &= 0.178454, \qquad \lambda_* = -0.022766, \\ A_H &= 0.277775, \qquad \Omega_H = 0.188519. \end{aligned} \tag{13}$$

The EP is 1.13×10^{-4} beyond the saddle-node but 9.93×10^{-2} before Hopf. In the original (r, ψ) coordinates, the Jacobian evaluated at the unrounded EP is displayed, rounded, as

$$J_* = \begin{pmatrix} 0.0098742542 & 0.0684808184 \\ -0.0155570989 & -0.0554055394 \end{pmatrix}. \tag{14}$$

Using the unrounded J_* and $\lambda_* = \mathrm{tr}\, J_*/2$ to form $N_* = J_* - \lambda_* I$, rather than subtracting the printed six-decimal eigenvalue from the printed matrix, the singular values are 8.40×10^{-2} and 1.7×10^{-17}, $\mathrm{rank}\, N_* = 1$, and $\|N_*^2\|_F = 2.0 \times 10^{-18}$. The double eigenvalue therefore has a one-dimensional eigenspace. The discriminant crosses transversely with $d\mathcal{D}/dA = -9.84226$ under stencil refinement, and the boundary-transverse eigenvalue is -0.16318. The locked state is consequently hyperbolic and stable throughout the three-dimensional OA phase quotient at the degeneracy.

Figure 2 combines the spectral tests for defectiveness with the corresponding change in the reduced radial relaxation response.

At the EP, $N_*^2 = 0$ gives the exact propagator

$$\mathrm{e}^{J_* t} = \mathrm{e}^{\lambda_* t}(I + t N_*). \tag{15}$$

For a small radial coherence perturbation $r \mapsto r + \epsilon$ at fixed phase, representative responses at a nearby node, at the EP, and at a nearby focus are

$$\begin{aligned} \text{node:}\quad & 1.8674\mathrm{e}^{-0.010939t} \\ & \quad - 0.8674\mathrm{e}^{-0.034852t}, \\ \text{EP:}\quad & \mathrm{e}^{-0.022766t}(1 + 0.032640t), \\ \text{focus:}\quad & \mathrm{e}^{-0.021371t}\cos(0.039641t) \\ & \quad + 0.8069\mathrm{e}^{-0.021371t}\sin(0.039641t). \end{aligned} \tag{16}$$

Here every expression denotes the linear response $\delta r(t)/\epsilon$; coefficients and rates are rounded. The node and focus parameters are those in Fig. 2(c). More precisely, writing $d = A_{\mathrm{EP}} - A_{\mathrm{SN}}$, they are $A_{\mathrm{EP}} - 0.45d$ and $A_{\mathrm{EP}} + 12d$, respectively. The node and EP traces have a small overshoot and are nonoscillatory, not monotone. The reported optimal two-component state gain is $G_{\max} = \sup_{t \geq 0} \sup_{v \neq 0} \|\mathrm{e}^{Jt} v\|_2 / \|v\|_2$ in the Euclidean (r, ψ) coordinates, not the order-parameter metric. The sampled time-grid estimates are approximately 1.520, 1.466, and 1.221 for these three samples; thus defectiveness does not maximize amplification here. Nonlinear signed-pulse integrations approach the small-signal form as the amplitude decreases. For $|\epsilon| \leq 10^{-3}$, the archived sweep has maximum relative time-integrated L^2 errors of 7.80%, 5.93%, and 2.11% for node, EP, and focus (Online Resource 1, Sects. S3.2 and S8).

4.1 Observable response and detection limits

For the radial input and output, the Laplace-domain transfer function is

$$R(s) = \mathbf{e}_1^{\mathsf{T}}(sI - J)^{-1}\mathbf{e}_1 = \frac{s - J_{22}}{s^2 - (\mathrm{tr}\, J)s + \det J}, \tag{17}$$

where $\mathbf{e}_1 = (1, 0)^{\mathsf{T}}$. At the EP it has a nonvanishing double-pole term $N_{*,11}/(s - \lambda_*)^2$, with $N_{*,11} = 0.032639897$. Equivalently, if $q(t) = \delta r(t)/\epsilon$ and $\tau = \mathrm{tr}\, J/2$, then the demodulated linear response $u(t) = \mathrm{e}^{-\tau t} q(t)$ satisfies

$$u''(t) = \tfrac{1}{4}\mathcal{D}\, u(t). \tag{18}$$

It is affine at the EP, hyperbolic on the node side, and sinusoidal on the focus side. This supplies a precise ideal diagnostic for the same observable, not a claim of noise-independent identification. As $\mathcal{D} \to 0$, all three forms become arbitrarily similar on a fixed observation window. In practice one should fit the full family in Eq. (17), sweep A, and test pulse-amplitude and observation-window dependence; visually fitting $t\mathrm{e}^{\lambda_* t}$ to one noisy trace is insufficient. The calibrated unrounded EP parameter and finite negative decay rate distinguish this transient crossover from the later self-sustained oscillation.

The radial operation is not a uniform phase shift. It can be realized on the OA manifold by a brief alignment field $h(t)\sin(\Phi_2 - \theta_j^{(2)})$ referenced to the instantaneous phase Φ_2. If

$$\kappa = 2\{\mathrm{artanh}(r + \epsilon) - \mathrm{artanh}(r)\}, \tag{19}$$

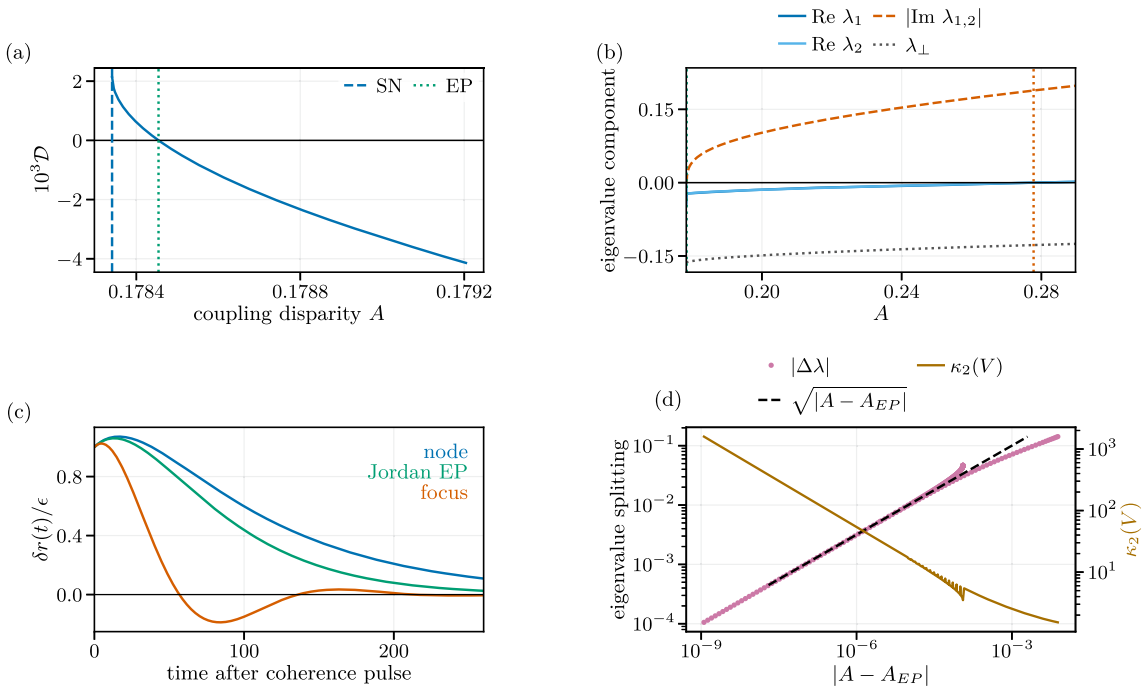


Fig. 2 Defective node–focus transition and relaxation at $\beta = 0.10$. **a** The plotted quantity is $10^3\mathcal{D}$; its zero occurs at the EP after the saddle-node (SN). Dashed and dotted vertical markers identify SN and EP. **b** The eigenvalue real parts remain negative through coalescence into a complex pair; $\lambda_\perp$ is the eigenvalue normal to the coherent boundary, and the later Hopf bifurcation (H) occurs when the real part reaches zero. **c** The linear normalized coherence response $\delta r(t)/\epsilon$ changes from a nonoscillatory bi-exponential return (node) to a Jordan response (EP) and then to a damped oscillation (focus). The respective parameters are $A = 0.178403224360$, $A_{\mathrm{EP}} \simeq 0.178454214878$, and $A = 0.179813962014$; all start from $(\delta r, \delta\psi) = (\epsilon, 0)$. The central trace uses the unrounded augmented EP solve, not the rounded parameter label. These curves represent the OA linearization. **d** $|\Delta\lambda|$ denotes the eigenvalue separation and $\kappa_2(V)$ the two-norm condition number of the eigenvector matrix V; the left and right axes display these quantities against $|A - A_{\mathrm{EP}}|$. The dashed square-root guide and divergent condition number diagnose coalescence, using Euclidean-normalized eigenvectors in (r, ψ)

the impulse maps r to $r + \epsilon$ without rotating the population phase. Equivalently, for $u_j = \exp[\mathrm{i}(\theta_j^{(2)} - \Phi_2)]$,

$$u_j^+ = \frac{u_j + a}{1 + a u_j}, \qquad a = \frac{(r+\epsilon) - r}{1 - r(r+\epsilon)}. \tag{20}$$

Finite Poisson-prepared ensembles approximate this instantaneous reset. For the archived reset test, the Poisson-kernel parameter is taken from the $\Delta = 10^{-3}$ EP. At $N = 4096$, 12 seeds and a target coherence increment 10^{-3} give root-mean-square amplitude error 2.43×10^{-5} and phase shift 2.68×10^{-5} radians (Online Resource 1, Sects. S3.3 and S8). These tests evaluate the reset map only; they do not integrate and verify microscopic node/EP/focus relaxation. In particular, the exact Jordan trace remains a statement about the OA linearization.

Recent circuit experiments demonstrate measurable EP-dependent responses with unidirectional coupling [40], although that mechanism differs from the reciprocal chimera considered here. A prospective implementation is an array of phase-resolved electronic oscillators with digitally programmed reciprocal intra- and inter-population coupling. A controller can estimate the second population's mean phase, apply the short sinusoidal alignment field above, and record its coherence and relative phase after switching the field off. This is a controlled response measurement, not spontaneous forcing or a completed experiment. Finite pulse duration, waveform harmonics, frequency mismatch, finite-N fluctuations, and parameter calibration would need separate validation.

5 The later Hopf bifurcation creates breathing

At A_H the complex pair that formed at the EP crosses the imaginary axis with $d\,\mathrm{Re}\,\lambda/dA = 0.151854 \neq 0$. Using the standard convention [41],

$$\ell_1 = \frac{\mathrm{Re}\, G_{21}}{2\Omega_H} = -0.3355 \qquad (\beta = 0.10), \tag{21}$$

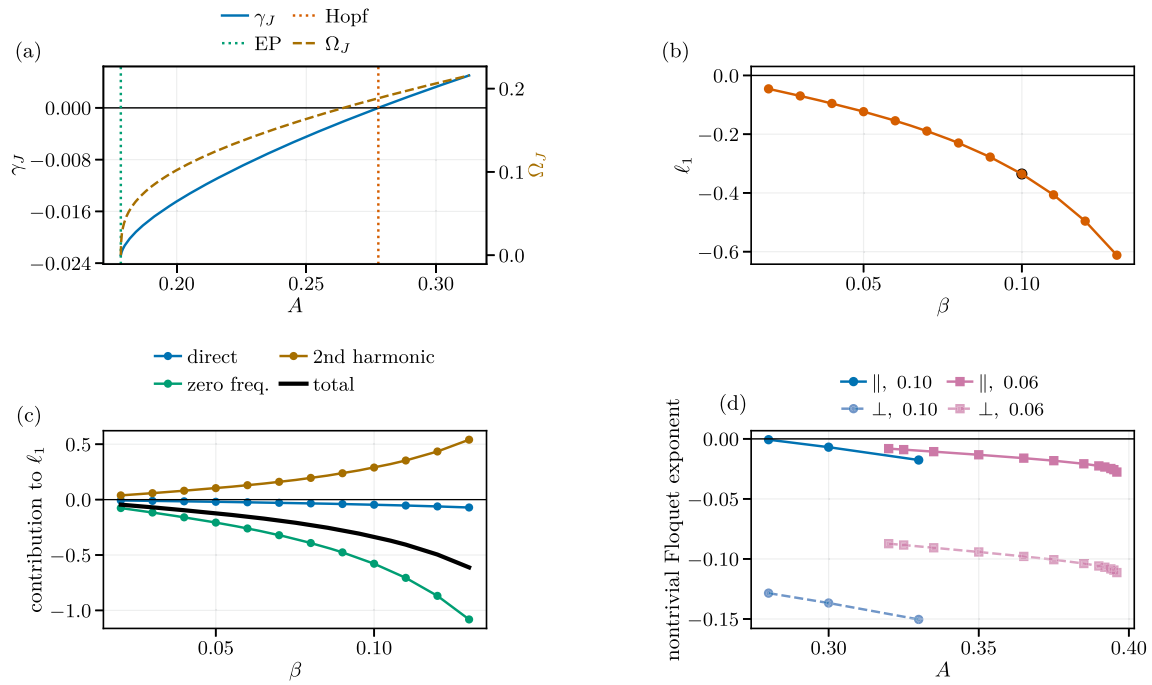


Fig. 3 Hopf onset and breathing-cycle stability in the Ott–Antonsen (OA) phase quotient. **a** $\gamma_J = \mathrm{Re}\,\lambda$ and $\Omega_J = |\mathrm{Im}\,\lambda|$ are the growth rate and angular frequency of the tracked pair; the exceptional point (EP) marks their earlier coalescence, and γ_J reaches zero only at the Hopf bifurcation. The solid left-axis curve is γ_J and the dashed right-axis curve is Ω_J; μ is reserved for the within-population coupling. **b** The first Lyapunov coefficient ℓ_1 is negative along the sampled Hopf locus, classifying it as supercritical. **c** "direct", "zero freq.", and "2nd harmonic" are $\mathrm{Re}\,G_{21}^{(c,0,2)}/(2\Omega_H)$ in Eq. (22). They describe cubic feedback and quadratic feedback via the zero-frequency and second-harmonic responses; their sum is the solid total ℓ_1. **d** $\Lambda_\parallel$ and $\Lambda_\perp$ are the nontrivial in-boundary and boundary-normal Floquet exponents; both are negative for the sampled cycles at $\beta = 0.10$ and 0.06. Solid and dashed curves denote the parallel and normal directions; circles and squares denote the two β slices. Connecting lines guide the eye between sampled cycles

so the Hopf bifurcation is supercritical. Polynomial-order, stencil, and step-size sensitivity tests preserve the sign, and ℓ_1 remains negative on the sampled Hopf locus.

For the decomposition in Fig. 3(c), expand the planar vector field as $F(x_H+\xi) = J_H\xi + \mathcal{B}(\xi,\xi)/2 + \mathcal{C}(\xi,\xi,\xi)/6 + \cdots$, where $\mathcal{B}$ and $\mathcal{C}$ are the second- and third-derivative multilinear forms. Choose $J_H q = \mathrm{i}\Omega_H q$, $J_H^{\mathsf{T}} p = -\mathrm{i}\Omega_H p$, $q^* q = 1$, and $p^* q = 1$. Define

$$
\begin{aligned}
G_{21}^{(c)} &= \langle p, \mathcal{C}(q,q,\bar{q})\rangle,\\
G_{21}^{(0)} &= -2\langle p, \mathcal{B}(q, J_H^{-1}\mathcal{B}(q,\bar{q}))\rangle,\\
G_{21}^{(2)} &= \langle p, \mathcal{B}(\bar{q}, (2\mathrm{i}\Omega_H I - J_H)^{-1}\mathcal{B}(q,q))\rangle.
\end{aligned}
\tag{22}
$$

Here $\langle p, v\rangle = p^* v$ and $G_{21} = G_{21}^{(c)} + G_{21}^{(0)} + G_{21}^{(2)}$. The plotted contributions are their real parts divided by $2\Omega_H$: respectively direct cubic feedback, quadratic feedback through the zero-frequency response, and quadratic feedback through the second harmonic.

For a boundary cycle of period T, the autonomous in-boundary multiplier is one. The remaining in-boundary and boundary-normal Floquet exponents are

$$
\Lambda_\parallel = \frac{1}{T}\int_0^T \mathrm{tr}\, J(t)\, dt, \qquad \Lambda_\perp = \frac{1}{T}\int_0^T \lambda_\perp(t)\, dt. \tag{23}
$$

Both are negative on every sampled breathing cycle at $\beta = 0.10$ and 0.06. At $\beta = 0.10$, $\Lambda_\parallel$ changes from -6.77×10^{-4} at $A = 0.28$ to -1.7602×10^{-2} at $A = 0.33$, while $\Lambda_\perp$ changes from -0.12846 to -0.15038. Direct monodromy integration agrees with Liouville's formula and recovers the trivial multiplier. Thus the sampled breathers attract in every nontrivial direction of the three-dimensional OA phase quotient. The conclusion remains subject to the zero-dispersion OA/Watanabe–Strogatz qualification in Sect. 2.

Figure 3 separates this later loss of stability from the earlier EP and summarizes the Lyapunov-coefficient and Floquet checks.

Table 1 Critical parameters at $\beta = 0.10$, $\Delta = 0$ and conservative empirical numerical sensitivity allowances. The allowance applies to the reference parameter, not to its six-decimal narrative label. Full refinement tables are provided in Online Resource 1, Sects. S3.7 and S7

Event	Reference parameter	Empirical allowance	Main check
Saddle-node	0.178340902616	10^{-10}	Solver and arithmetic refinement
EP	0.178454214878	10^{-10}	Solver and arithmetic refinement
Hopf	0.277775484648	10^{-10}	Solver and arithmetic refinement
Homoclinic	0.353696543821	2×10^{-10}	Solver, section, launch refinement

6 High-accuracy numerical identification of homoclinic termination

We continued the attracting cycle on the same fixed-β parameter slice. At each A, the lower-coherence unstable branch of the saddle was integrated forward and its stable branch backward to the transverse section $r = r_{\mathrm{sec}}$. The section splitting changes sign at

$$A_{\mathrm{hom}} = 0.353697. \tag{24}$$

At the connection, the saddle has $(r_s, \psi_s) = (0.945412, -0.298999)$, $\lambda_u = 0.0533964$, and $\lambda_s = -0.104515$, giving a negative saddle quantity. The continued period grows from 191.929 at $A = 0.353680$ to 255.889 at $A = 0.353696$. With the independently shot endpoint fixed, the last six points follow

$$T = C - c \log(A_{\mathrm{hom}} - A), \tag{25}$$

with $c^{-1} = 0.0533948$, within 2.97×10^{-5} relative to λ_u, as expected for period growth near a one-saddle homoclinic orbit [41, 42].

The logarithmic residual is much smaller than that of an equal-parameter saddle-node-on-invariant-circle fit, and the conclusion persists across terminal windows. This small-sample corrected Akaike information criterion (AICc) comparison [43] is descriptive because the continuation points are deterministic and related. Solver-tolerance and maximum-step refinement changes the computed shooting root by less than 2×10^{-10}, while section and launch-distance changes are smaller. Narrative labels use six decimals; Table 1 gives reference parameters and empirical allowances, and machine-readable files retain the full stored precision. The result is a high-accuracy numerical identification, not a computer-assisted proof.

Figure 4 assembles the independent manifold-shooting, period-scaling, and fitting-window evidence for this numerical identification.

7 Parameter dependence and robustness

Continuation in β places the EP between the saddle-node and Hopf bifurcations throughout $0.02 \le \beta \le 0.22$. The saddle-node–EP gap collapses toward the Bogdanov–Takens (BT) point

$$\begin{aligned}(\beta_{\mathrm{BT}}, A_{\mathrm{BT}}) &= (0.223916, 0.337203),\\ (r_{\mathrm{BT}}, \psi_{\mathrm{BT}}) &= (0.658983, -\pi/6).\end{aligned} \tag{26}$$

The resulting codimension-one loci and their approach to the BT endpoint are shown in Fig. 5(a–c). This endpoint is the expected exception to the strict sign-change setting of Lemma 1, because the second eigenvalue at the saddle-node also vanishes. The nonzero quadratic BT coefficients and regular parameter unfolding are documented in Online Resource 1.

More importantly for physical scope, we repeated the continuation with a common positive Lorentzian half-width Δ in the full three-dimensional quotient (ρ_1, ρ_2, ψ). The exactly coherent boundary then disappears. At $\Delta = 10^{-3}$,

$$\begin{aligned}A_{\mathrm{SN}} &= 0.180443, \qquad A_{\mathrm{EP}} = 0.180620,\\ A_H &= 0.286121.\end{aligned} \tag{27}$$

At the EP, the repeated eigenvalue is -0.024284, the isolated third eigenvalue is -0.162539, and the singular values of $J - \lambda_* I$ are 0.215642, 0.076519, and 3.8×10^{-17}. The double eigenvalue remains defective and all three modes remain stable. The ordering $A_{\mathrm{SN}} < A_{\mathrm{EP}} < A_H$ holds at all 21 sampled values over $0 \le \Delta \le 0.005$ (Fig. 5(d)). This continuation leaves the exactly coherent boundary and the identical-frequency Watanabe–Strogatz limit while retaining the same ordering within the OA quotient. It does not test attraction from arbitrary frequency-dependent initial densities.

Two subordinate tests further delimit generalization. In controlled $M = 4$ and $M = 5$ population rings, the metric-aware ordered real-Schur construction isolates a two-mode plane and locates stable defective transitions while the remaining modes stay spectrally separated. These are linear spectral benchmarks, not new chimera solutions. A

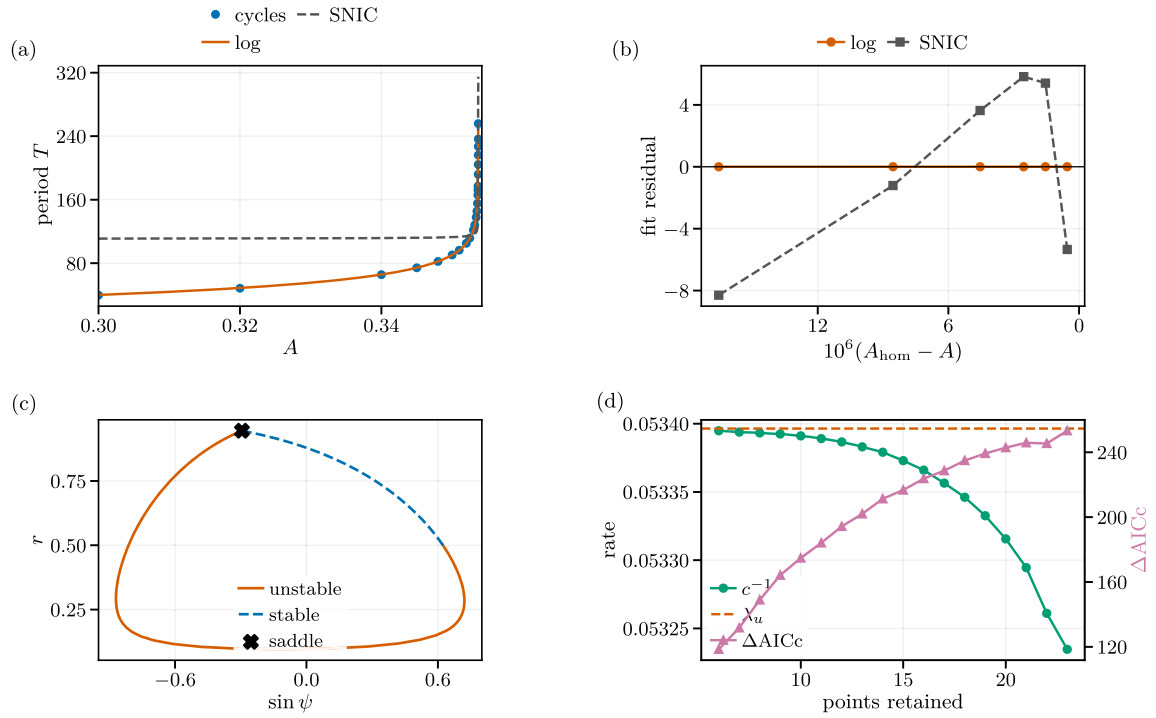


Fig. 4 Homoclinic termination on the fixed $\beta = 0.10$ parameter slice. **a** Breathing-cycle periods T diverge toward the independently shot homoclinic parameter A_{hom}. **b** The logarithmic law in Eq. (25) is compared with saddle-node-on-invariant-circle (SNIC) scaling; ΔAICc is the difference in the small-sample corrected Akaike information criterion. **c** The forward unstable and backward stable saddle manifolds meet on a transverse section to form the same loop. **d** The fitted inverse logarithmic coefficient c^{-1} agrees with the unstable saddle eigenvalue λ_u across terminal fitting windows, while the AICc advantage remains positive. Here positive $\Delta\mathrm{AICc} = \mathrm{AICc}_{\mathrm{SNIC}} - \mathrm{AICc}_{\mathrm{log}}$ favors logarithmic scaling. In (c), the matching section is $r = 0.5$ and the reference launch distance from the saddle is 10^{-7}. The terminal six-point window spans $0.353680 \le A \le 0.353696$; Table 1 gives the empirical uncertainty of the independently shot endpoint

normal circulant counterexample confirms that a nonzero skew-adjoint component, non-normality, and defectiveness are distinct properties. Separately, finite-N simulations at $A = 0.33$, $\beta = 0.10$ use independent Poisson-kernel samples for $64 \le N \le 2048$. Their exact chordal quotient distance from the OA cycle scales as $N^{-0.501}$ with a conditional seed-bootstrap interval $[-0.542, -0.460]$; step halving gives -0.496. These details and Figs. S3–S4 are provided in Online Resource 1. Since $A = 0.33$ is above Hopf, this finite-N result validates the sampled OA breathing cycle for the specified preparation, not the pre-Hopf relaxation in Fig. 2(c). Neither the exponent nor its conditional bootstrap interval is a proof of generic OA attraction.

8 Numerical methods and reproducibility

Critical points were found as roots of augmented nonlinear systems rather than read from parameter grids. Equilibrium residuals were required to be below 10^{-9} in the infinity norm and were typically near machine precision. The finite-difference condition numbers of the augmented saddle-node, EP, and Hopf systems were 4.07, 8.37, and 13.88, respectively. The β loci used steps of 0.005; the EP derivative was checked under centered-stencil refinement. For $M > 2$, ordered real-Schur frames were aligned by orthogonal Procrustes transformations, and invariance residuals and spectral gaps were recorded.

Cycle and variational equations were integrated with the eighth-order DOP853 method [44]. Monodromy closure, the trivial multiplier, and Liouville consistency were checked explicitly; the achieved near-Hopf period coefficient of variation was below 10^{-8} and was smaller at points farther from Hopf. The first Lyapunov coefficient was checked over polynomial degrees 5–7, grids from 7^2 to 11^2, and differentiation scales $0.005 \le h \le 0.06$. Homoclinic shooting used the documented section and launch-distance ensemble together with independent tolerance and maximum-step refinement. Finite-N uncertainty was estimated by a stratified seed bootstrap. Main-text digits were limited by these sensitivity tests rather than by nonlinear residuals alone.

8.1 Numerical sensitivity and reported digits

Table 1 makes the parameter error budget explicit. For SN, EP, and Hopf we solved $F = 0$ together with $\det J = 0$, $\mathcal{D} = 0$, or $\mathrm{tr}\, J = 0$, respectively, at nonlinear solver tolerances 10^{-8}, 10^{-10}, and 10^{-12} with three nearby initial

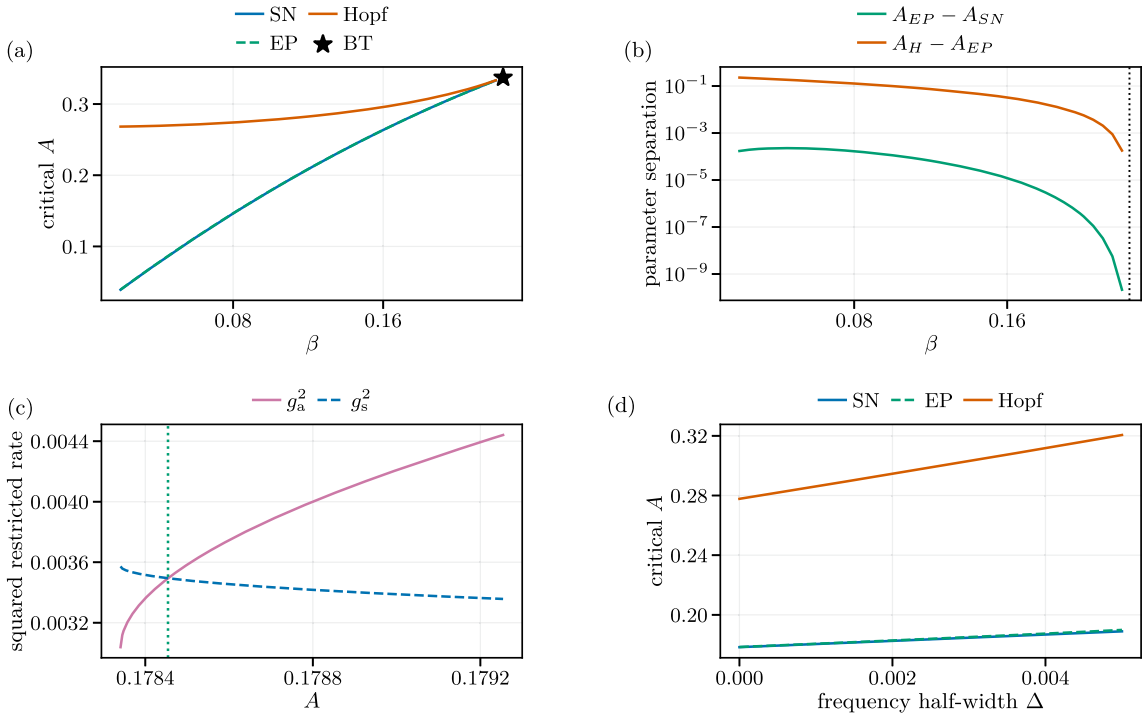


Fig. 5 Parameter dependence and positive-dispersion robustness. **a** Saddle-node bifurcation (SN), exceptional point (EP), and Hopf bifurcation (H) loci in (β, A); the star marks the Bogdanov–Takens (BT) point. **b** The EP–SN and H–EP parameter separations decrease toward BT. **c** g_a is the magnitude of the skew-adjoint component and g_s the magnitude of the traceless self-adjoint component of the restricted Jacobian in the declared order-parameter metric; they are equal at the EP. **d** The three event loci remain ordered as the common Lorentzian frequency half-width Δ is increased from zero. Panel (a) samples $0.02 \le \beta \le 0.22$; in (b) the differences are $A_{\mathrm{EP}} - A_{\mathrm{SN}}$ and $A_H - A_{\mathrm{EP}}$. Panel (d) uses $\beta = 0.10$ and 21 values of $0 \le \Delta \le 0.005$. Equality in (c) locates the same EP for every positive-definite metric on the tracked space

guesses. Independent 30-, 50-, and 80-decimal-digit solves use the analytic vector field and arbitrary-precision derivatives. The maximum observed double-precision deviations from the 80-digit reference were 6.09×10^{-13}, 1.08×10^{-13}, and 2.63×10^{-13}, respectively. We assign a conservative 10^{-10} empirical allowance to each local event. For the homoclinic endpoint, the existing five-level DOP853 refinement varies (rtol, atol, $h_{\max}$) from $(3 \times 10^{-9}, 3 \times 10^{-11}, 0.6)$ to $(10^{-12}, 10^{-14}, 0.05)$, and a separate 16-case sweep varies section and launch distance. The observed root spans are 1.50×10^{-11} and 2.21×10^{-13}, respectively; the conservative allowance remains 2×10^{-10}. Online Resource 1, Sects. S3.7, S7, and S9, gives the complete settings, output tables, and provenance.

These are deterministic sensitivity allowances, not statistical confidence intervals or certified enclosures. They exclude uncertainty in physical model parameters. Six-decimal labels in the narrative and schematics have an additional rounding error of at most 5×10^{-7}; they must not be used to reproduce an exact Jordan trace. The extra digits in Table 1 identify numerical reference values without claiming that every printed digit is experimentally meaningful.

The public reproducibility release contains source tables, analytic Jacobians, nonlinear pulse tests, Floquet validation, manifold shooting, positive-dispersion continuation, larger-population examples, a normal counterexample, finite-N analysis, figure code, and a validation driver. The default command reconstructs the analyses and figures from the archived raw finite-N tables; an explicit full mode regenerates the computationally expensive oscillator ensembles.

9 Discussion

The result is a precise separation of two events. On the fixed $\beta = 0.10$ slice, the stable locked branch reaches a defective node–focus transition at $A_{\mathrm{EP}} = 0.178454$, where a negative eigenvalue pair and its eigenvectors coalesce. The equilibrium remains hyperbolic and stable; only the form of its return changes. Breathing begins much later, at the established Hopf bifurcation $A_H = 0.277775$. The negative first Lyapunov coefficient and negative nontrivial OA-quotient Floquet exponents characterize the emergent stable breather, which then approaches the numerically identified homoclinic termination at $A_{\mathrm{hom}} = 0.353697$.

The discriminant lemma places this result in standard nonlinear-dynamics language. When the same planar pair is real at a generic saddle-node and purely imaginary at Hopf, a node–focus boundary is structurally expected under the stated isolation and continuity assumptions. Calling its trans-

verse, non-scalar realization an exceptional point emphasizes the verified defectiveness of the Jacobian; it does not create a new bifurcation mechanism. The physical value is that an unchanged locked macroscopic state can have distinct recovery dynamics: two decaying modes, a defective return, or damped collective ringing. The radial transfer function quantifies this distinction and gives a nonzero Jordan contribution to a directly defined coherence observable. It does not establish a causal influence of the EP on the Hopf threshold or its normal-form coefficient.

This positioning builds on, rather than replaces, earlier work. Ryu et al. [32] already associated Jacobian exceptional points with reorganized transients in coupled dissipative oscillators approaching amplitude death. Asir [33] connected exceptional points and symmetry breaking to chimera emergence in a nonreciprocal Stuart–Landau system. Here the population coupling is reciprocal, the locked chimera already exists, and the coalescing pair remains strictly stable and isolated from the boundary-normal mode. Its location and return law are resolved separately from the established Hopf creation of breathing. No new generic node–focus mechanism is claimed.

The positive-dispersion calculation strengthens but does not overextend the scope. It shows that the event ordering and defectiveness persist when the exact coherent boundary and the identical-frequency Watanabe–Strogatz degeneracy are removed. The zero-dispersion finite-N test remains conditional on Poisson-kernel preparation, and the narrow saddle-node–EP interval makes the Jordan trace parameter-sensitive. Accordingly, the pulse construction and detection protocol identify what to measure and how to prepare the input, while the closure-defect bound states one finite-time condition for trusting the reduced response. The bound does not predict that non-Poisson defects decay. Post-pulse microscopic relaxation across different Watanabe–Strogatz leaves, parameter-estimation uncertainty, and an experimental implementation remain open. These limitations are especially relevant because nearby node, EP, and focus signals cannot be distinguished arbitrarily close to coalescence at finite observation time and finite noise.

Supplementary information

The revised Online Resource 1 is supplied as a complete supplementary document. Sections S1–S4 contain the theoretical derivations, analytic Jacobians, numerical protocols, nonlinear OA pulse tests, instantaneous microscopic-reset checks, Floquet and homoclinic validation, positive-dispersion continuation, larger-population benchmarks, and finite-N breathing-cycle analysis. Sections S5–S9 add the closure-defect estimate, alternative-metric checks, local parameter-refinement tables, precise pulse and gain conventions, and a source-to-figure map. The companion reproducibility archive contains the executable revision checks and their outputs, the revised supplementary source, and the figure-label update. Newly computed checks are distinguished from the existing archived data.

Supplementary Information The online version contains supplementary material available at https://doi.org/10.1007/s11071-026-13128-w.

Author Contributions E.B. conceived the study, developed the theoretical framework, performed the formal and numerical analyses, prepared the figures and reproducibility package, and drafted the manuscript and Supplementary Information. S.H.A. contributed to conceptual discussion, supervision, interpretation, and critical revision. M.P. contributed to supervision, interpretation, funding acquisition, and critical revision.

Funding This work was partially supported by Metasan (Tadbirgaran Kimia Pishtaz Co.) under Research Grant No. TKP-GRANT-M260601. M.P. was supported by the Slovenian Research and Innovation Agency under Grant No. P1-0403.

Data availability The code, data, and figures required to reproduce the numerical results reported in this study are openly available. The revised reproducibility package (v1.1.2) is archived on Zenodo at https://doi.org/10.5281/zenodo.22861483 and developed in the associated GitHub repository https://github.com/EhsanBolhasani/stable-ep-before-hopf-reproducibility. It contains the source data, analysis and figure-generation code, LaTeX sources, and validation workflow, with a SHA-256 manifest. The baseline v1.0.0 archive remains available at https://doi.org/10.5281/zenodo.21828808; this DOI identifies the original release only. No external datasets were used.

Declarations

Conflict of interest The authors have no relevant financial or non-financial interests to disclose.

References

1. Kuramoto, Y., Battogtokh, D.: Coexistence of coherence and incoherence in nonlocally coupled phase oscillators. Nonlinear Phenom. Complex Syst. **5**, 380–385 (2002)
2. Abrams, D.M., Strogatz, S.H.: Chimera states for coupled oscillators. Phys. Rev. Lett. **93**, 174102 (2004). https://doi.org/10.1103/PhysRevLett.93.174102
3. Abrams, D.M., Strogatz, S.H.: Chimera states in a ring of nonlocally coupled oscillators. Int. J. Bifurcat. Chaos **16**(1), 21–37 (2006). https://doi.org/10.1142/S0218127406014551
4. Laing, C.R.: The dynamics of chimera states in heterogeneous Kuramoto networks. Physica D **238**, 1569–1588 (2009). https://doi.org/10.1016/j.physd.2009.04.012
5. Bera, B.K., Majhi, S., Ghosh, D., Perc, M.: Chimera states: effects of different coupling topologies. EPL **118**(1), 10001 (2017). https://doi.org/10.1209/0295-5075/118/10001
6. Panaggio, M.J., Abrams, D.M.: Chimera states: coexistence of coherence and incoherence in networks of coupled oscillators. Nonlinearity **28**, R67–R87 (2015). https://doi.org/10.1088/0951-7715/28/3/R67
7. Omel'chenko, O.E.: The mathematics behind chimera states. Nonlinearity **31**, R121–R164 (2018). https://doi.org/10.1088/1361-6544/aaaa07

8. Parastesh, F., Jafari, S., Azarnoush, H., Shahriari, Z., Wang, Z., Boccaletti, S., Perc, M.: Chimeras. Phys. Rep. **898**, 1–114 (2021). https://doi.org/10.1016/j.physrep.2020.10.003
9. Haugland, S.W.: The changing notion of chimera states, a critical review. J. Phys. Complex. **2**, 032001 (2021). https://doi.org/10.1088/2632-072X/ac0810
10. Hagerstrom, A.M., Murphy, T.E., Roy, R., Hövel, P., Omelchenko, I., Schöll, E.: Experimental observation of chimeras in coupled-map lattices. Nat. Phys. **8**, 658–661 (2012). https://doi.org/10.1038/nphys2372
11. Tinsley, M.R., Nkomo, S., Showalter, K.: Chimera and phase-cluster states in populations of coupled chemical oscillators. Nat. Phys. **8**, 662–665 (2012). https://doi.org/10.1038/nphys2371
12. Martens, E.A., Thutupalli, S., Fourrière, A., Hallatschek, O.: Chimera states in mechanical oscillator networks. Proc. Natl. Acad. Sci. U.S.A. **110**, 10563–10567 (2013). https://doi.org/10.1073/pnas.1302880110
13. Montbrió, E., Kurths, J., Blasius, B.: Synchronization of two interacting populations of oscillators. Phys. Rev. E **70**(5), 056125 (2004). https://doi.org/10.1103/PhysRevE.70.056125
14. Abrams, D.M., Mirollo, R., Strogatz, S.H., Wiley, D.A.: Solvable model for chimera states of coupled oscillators. Phys. Rev. Lett. **101**, 084103 (2008). https://doi.org/10.1103/PhysRevLett.101.084103
15. Wolfrum, M., Omel'chenko, O.E., Yanchuk, S., Maistrenko, Y.L.: Spectral properties of chimera states. Chaos **21**(1), 013112 (2011). https://doi.org/10.1063/1.3563579
16. Panaggio, M.J., Abrams, D.M., Ashwin, P., Laing, C.R.: Chimera states in networks of phase oscillators: The case of two small populations. Phys. Rev. E **93**(1), 012218 (2016). https://doi.org/10.1103/PhysRevE.93.012218
17. Laing, C.R.: Dynamics and stability of chimera states in two coupled populations of oscillators. Phys. Rev. E **100**(4), 042211 (2019). https://doi.org/10.1103/PhysRevE.100.042211
18. Bolotov, M.I., Smirnov, L.A., Osipov, G.V., Pikovsky, A.S.: Breathing chimera in a system of phase oscillators. JETP Lett. **106**, 393–399 (2017). https://doi.org/10.1134/S0021364017180059
19. Omel'chenko, O.E.: Mathematical framework for breathing chimera states. J. Nonlinear Sci. **32**, 22 (2022). https://doi.org/10.1007/s00332-021-09779-1
20. Ott, E., Antonsen, T.M.: Low dimensional behavior of large systems of globally coupled oscillators. Chaos **18**, 037113 (2008). https://doi.org/10.1063/1.2930766
21. Ott, E., Antonsen, T.M.: Long time evolution of phase oscillator systems. Chaos **19**, 023117 (2009). https://doi.org/10.1063/1.3136851
22. Watanabe, S., Strogatz, S.H.: Integrability of a globally coupled oscillator array. Phys. Rev. Lett. **70**, 2391–2394 (1993). https://doi.org/10.1103/PhysRevLett.70.2391
23. Pikovsky, A., Rosenblum, M.: Partially integrable dynamics of hierarchical populations of coupled oscillators. Phys. Rev. Lett. **101**, 264103 (2008). https://doi.org/10.1103/PhysRevLett.101.264103
24. Marvel, S.A., Mirollo, R.E., Strogatz, S.H.: Identical phase oscillators with global sinusoidal coupling evolve by Möbius group action. Chaos **19**, 043104 (2009). https://doi.org/10.1063/1.3247089
25. Engelbrecht, J.R., Mirollo, R.: Is the Ott-Antonsen manifold attracting? Phys. Rev. Research **2**, 023057 (2020). https://doi.org/10.1103/PhysRevResearch.2.023057
26. Lee, S., Krischer, K.: Attracting Poisson chimeras in two-population networks. Chaos **31**, 113101 (2021). https://doi.org/10.1063/5.0065710
27. Martens, E.A., Panaggio, M.J., Abrams, D.M.: Basins of attraction for chimera states. New J. Phys. **18**(2), 022002 (2016). https://doi.org/10.1088/1367-2630/18/2/022002
28. Rakshit, S., Bera, B.K., Perc, M., Ghosh, D.: Basin stability for chimera states. Sci. Rep. **7**, 2412 (2017). https://doi.org/10.1038/s41598-017-02409-5
29. Kato, T.: Perturbation Theory for Linear Operators. Springer, Berlin (1995). https://doi.org/10.1007/978-3-642-66282-9
30. Heiss, W.D.: The physics of exceptional points. J. Phys. A: Math. Theor. **45**, 444016 (2012). https://doi.org/10.1088/1751-8113/45/44/444016
31. Miri, M.-A., Alù, A.: Exceptional points in optics and photonics. Science **363**, eaar7709 (2019). https://doi.org/10.1126/science.aar7709
32. Ryu, J.-W., Son, W.-S., Hwang, D.-U., Lee, S.-Y., Kim, S.W.: Exceptional points in coupled dissipative dynamical systems. Phys. Rev. E **91**(5), 052910 (2015). https://doi.org/10.1103/PhysRevE.91.052910
33. Asir, M.P.: Emergence of chimeras: An impetus by exceptional points. Phys. Rev. E **108**, 024220 (2023). https://doi.org/10.1103/PhysRevE.108.024220
34. Kreienkamp, K.L., Klapp, S.H.L.: Synchronization and exceptional points in nonreciprocal active polar mixtures. Commun. Phys. **8**, 307 (2025). https://doi.org/10.1038/s42005-025-02220-z
35. Kuramoto, Y.: Chemical Oscillations, Waves, and Turbulence. Springer, Berlin (1984). https://doi.org/10.1007/978-3-642-69689-3
36. Sakaguchi, H., Kuramoto, Y.: A soluble active rotator model showing phase transitions via mutual entrainment. Prog. Theor. Phys. **76**, 576–581 (1986). https://doi.org/10.1143/PTP.76.576
37. Pietras, B., Daffertshofer, A.: Ott-Antonsen attractiveness for parameter-dependent oscillatory networks. Chaos **26**, 103101 (2016). https://doi.org/10.1063/1.4963371
38. Ageeva, M.V., Goldobin, D.S.: Nonlinear bias of collective oscillation frequency induced by asymmetric Cauchy noise. Chaos **35**, 023126 (2025). https://doi.org/10.1063/5.0239363
39. Horn, R.A., Johnson, C.R.: Matrix Analysis, 2nd edn. Cambridge University Press, Cambridge (2012). https://doi.org/10.1017/CBO9781139020411
40. Zhao, W., Zhang, Y., Gao, Z., Peng, D., Kou, J.-L., Lu, Y.-Q., El-Ganainy, R., Özdemir, ŞK., Zhong, Q.: Exceptional points induced by unidirectional coupling in electronic circuits. Nat. Commun. **15**, 9907 (2024). https://doi.org/10.1038/s41467-024-53929-4
41. Kuznetsov, Y.A.: Elements of Applied Bifurcation Theory, 3rd edn. Springer, New York (2004). https://doi.org/10.1007/978-1-4757-3978-7
42. Glendinning, P., Sparrow, C.: Local and global behavior near homoclinic orbits. J. Stat. Phys. **35**, 645–696 (1984). https://doi.org/10.1007/BF01010828
43. Hurvich, C.M., Tsai, C.-L.: Regression and time series model selection in small samples. Biometrika **76**(2), 297–307 (1989). https://doi.org/10.1093/biomet/76.2.297
44. Hairer, E., Nørsett, S.P., Wanner, G.: Solving Ordinary Differential Equations I: Nonstiff Problems, 2nd edn. Springer Series in Computational Mathematics, vol. 8. Springer, Berlin (1993). https://doi.org/10.1007/978-3-540-78862-1

Publisher's Note Springer Nature remains neutral with regard to jurisdictional claims in published maps and institutional affiliations.

Springer Nature or its licensor (e.g. a society or other partner) holds exclusive rights to this article under a publishing agreement with the author(s) or other rightsholder(s); author self-archiving of the accepted manuscript version of this article is solely governed by the terms of such publishing agreement and applicable law.